Modeling of Transient Ionizing Radiation Effects in Bipolar Devices at High Dose-Rates

Tor. A. Fjeldly, *Fellow IEEE*, Yanqing Deng, Michael S. Shur, *Fellow IEEE*, Harold P. Hjalmarson, Arnoldo Muyshondt, Trond Ytterdal, *Member IEEE*

Abstract--**We have developed a dynamic model for photoelectric effect in bipolar devices exposed to a wide range of ionizing radiation intensities. We represent the stationary and dynamic photocurrents by current sources in parallel with each *p-n*-junction. These sources include the prompt photocurrent of the depletion regions, and the delayed response associated with the build-up and discharge of excess charge carriers in the quasi-neutral regions adjacent to the junctions. The latter are described in terms of dynamic delay times for each q-n region, which can be represented by RC equivalent delay circuits. The model has been implemented in the circuit simulator AIM-Spice, and has been verified by numerical simulations.**

Index Terms--**Circuit simulation, device modeling, ionizing radiation, photoelectric effect, semiconductor devices, transient phenomena.**

I. Introduction

To optimally design circuits for operation at high intensities of ionizing radiation, and to accurately predict their behavior under radiation, precise device models are needed that include both the stationary and dynamic effects of such radiation. Depending on the type and dose-rate of the ionizing radiation, different degradation mechanisms, such as photoelectric effect, total dose effect, or single even upset might be dominant [1], [2]. In this paper, we consider only the photoelectric effect associated with the generation of electron-hole pairs in the semiconductor.

The effects of low radiation intensity on *p-n* diodes and bipolar junction transistors (BJTs) were described by low-injection theory in the classical paper by Wirth and Rogers [3]. However, in BJTs compatible with modern integrated circuit technology, high-resistivity regions are often used to enhance device performance, either as a substrate or as an epitaxial layer such as the low-doped collector region of the device. Using low-injection theory, the transient response of epitaxial BJTs was discussed by Florian et al. [4], [5], who mainly concentrated on the effects of the Hi-Lo (high doping - low doping) epilayer/substrate junction of the collector, and on geometrical effects of realistic devices.

For devices with highly resistive regions, the assumption of low-level injection is often inappropriate, even at moderate radiation dose-rates, and a more complete theory for high injection levels was needed. In the dynamic photocurrent model by Enlow and Alexander [6], *p-n* junctions exposed to high-intensity radiation were considered. In their work, the variation of the minority carrier lifetime with excess carrier density, and the effects of the ohmic electric field in the quasi-neutral (q-n) regions were included in a simplified manner. Later, Wunsch and Axness [7], presented a more comprehensive model for the transient radiation response of *p-n* and *p-i-n* diode geometries. A stationary model for high-level injection in *p-n* junctions was developed by Isaque et al. [8]. They used a more complete ambipolar transport equation, which included the dependencies of the transport parameters (ambipolar diffusion constant, mobility, and recombination rate) on the excess minority carrier concentration. The expression used for the recombination rate was that of Shockley-Reed-Hall (SRH) recombination, which is dominant for low to high radiation intensities. However, at very high dose-rates, Auger recombination becomes important and will eventually be dominant.

The complete ambipolar transport equation, including the complicated dependence of transport parameters on the radiation intensity, cannot be solved analytically. We therefore seek an approximate solution for this equation in each of the regimes where a given recombination mechanism dominates, and then join these solutions by using appropriate smoothing functions. This approach allows us to develop diode and BJT models that account for the photoelectric effect in a wide range of dose-rates, and are suitable for implementation in circuit simulators such as SPICE.

The present model was verified by numerical simulations using the MEDICI device simulator [9].

II. Device Model

In circuit simulators such as SPICE, the device models are defined in terms of equivalent circuits consisting of circuit elements such as current sources, capacitances, resistances,

Manuscript received September 11, 2000. This work was supported in part by the Sandia National Laboratories under Grant No. A30259.

T. A. Fjeldly is with UniK - Center for Technology, Norwegian University of Science and Technology, Kjeller, Norway, and the ECSE Department, Rensselaer Polytechnic Institute, Troy, NY 12180-3590, USA (telephone: +47 6484 4747, e-mail: torfj@ unik.no).

Y. Deng, is with the ECSE Department, Rensselaer Polytechnic Institute, Troy, NY 12180-3590, USA (e mail: dengyq@rpi.edu) .

M. S. Shur is with the ECSE Department, Rensselaer Polytechnic Institute, Troy, NY 12180-3590, USA (shurm@rpi.edu)

H. P. Hjalmarson is with Sandia National Laboratories, Albuquerque, NM 87185, USA (hphjalm@sandia.gov).

A. Muyshondt is with Sandia National Laboratories, Albuquerque, NM 87185, USA (amuysho@sandia.gov).

T. Ytterdal is with the Department of Physical Electronics, Norwegian University of Science and Technology, Trondheim, Norway (ty@nvlsi.no).

etc. Adding suitable equivalent circuits for the photoelectric effect, such models can be used for simulating the dynamic behavior of irradiated devices. In the present model, we represent the stationary and dynamic photocurrents by means of a current source in parallel with each *p-n*-junction, as shown in Fig. 1 for the basic *p-n* diode (a) and for the Gummel-Poon BJT model (b) [10] - [12].

These current sources include the prompt photocurrent associated with the generation of electron-hole (e-h) pairs in the depletion regions, and the delayed response associated with the build-up and discharge of excess charge carriers in the q-n regions adjacent to the junctions. The latter are described in terms of a characteristic delay time for each q-n region, which can be represented by RC equivalent delay circuits, as shown in Fig. 1c. However, since the delay times (τ_{pd} and τ_{nd}) are given by the ambipolar transport parameters within the q-n regions, they will be dynamic quantities determined by the momentary amount of minority carrier within a so-called collection volume (effective diffusion length times junction area).

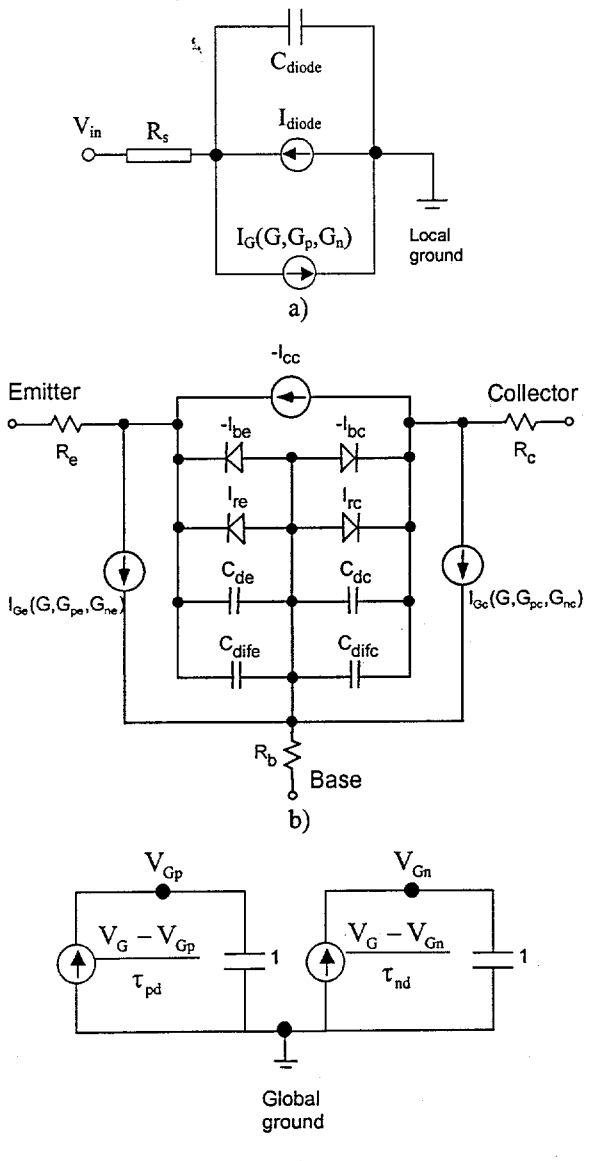

Fig. 1. Basic diode (a) and Gummel-Poon BJT (b) models including photocurrent sources I_{Gx} corresponding to the various *p-n* junctions. The temporal evolution of I_{Gx} is included through the dynamic quantities $G \equiv kV_G$, $G_{pe} \equiv kV_{Gpe}$, $G_{ne} \equiv kV_{Gne}$, etc., defined by delay subcircuits (c).

We denote the actual e-h generation rate by G, and use G_{xy} ($x = p$ or n, $y = e$ or c (BJT)) to represent effective generation rates corresponding to the momentary value of the excess minority carriers in the collection volume. V_{Gxy} are fictitious voltages corresponding to these generation rates, suitably scaled by a factor k to be within a normal range for circuit simulation.

A. Stationary Model

The photocurrent in a diode structure consists of three terms: the drift term for electron-hole pairs produced in the diode depletion region, and the ambipolar transport of charge carrier in the two q-n regions adjacent to the depletion region. The first term gives rise to a "prompt" current density $J_{depl} = qGW_{dep}$, where W_{dep} is the width of the depletion region. This current responds with a time constant given by the transport time $\tau_{dep} = W_{dep}/v$ across the depletion region, where v is the carrier drift velocity.

The photocurrent contributions from the q-n regions adjacent to the depletion region are governed by the ambipolar transport equation. At low radiation dose-rates (low-injection), the ambipolar transport parameters become independent of the dose-rate. This is also the case in the higher dose-rate regime where the SRH traps are saturated [6] - [8]. Hence, in both these regimes, the stationary ambipolar diffusion equation can be solved analytically for a one-dimensional *n-p* junction (with cross-section A), resulting in the following total photocurrent:

$$I_G = qAG\left(W_{dep} + L_{pd} + L_{nd}\right), \tag{1}$$

where

$$L_{pd} = L_{ap}\tanh\left(W_n/2L_{ap}\right), \tag{2}$$

$$L_{nd} = L_{an}\tanh\left(W_p/2L_{an}\right). \tag{3}$$

Here, G is the stationary e-h generation rate. L_{pd} and L_{nd} are effective diffusion lengths, L_{ap} and L_{an} are the ambipolar minority carrier diffusion lengths, and W_n and W_p are the lengths of the *n*-type and *p*-type q-n region, respectively. In these expressions, it is assumed that all minority carriers reaching the ohmic contacts of the diode recombine spontaneously.

The corresponding effective diffusion lengths in the Hi-Lo region of *p-n-n*$^+$ and *n-p-p*$^+$ diodes become [2], [3], [12]:

$$L_{pd} = L_{ap}\left[\tanh\left(\frac{W_n}{L_{ap}}\right) + \frac{L_{ap+}/L_{ap}}{\cosh\left(W_n/L_{ap}\right)}\right], \tag{4}$$

$$L_{nd} = L_{an}\left[\tanh\left(\frac{W_p}{L_{an}}\right) + \frac{L_{an+}/L_{an}}{\cosh\left(W_p/L_{an}\right)}\right], \tag{5}$$

where W_n and W_p now are the lengths of the low-doped regions and L_{ap+} and L_{an+} are the minority carrier diffusion lengths of

DISCLAIMER

DISCLAIMER

Portions of this document may be illegible in electronic image products. Images are produced from the best available original document.

the highly doped n-type and p-type q-n regions, respectively. The widths of the heavily doped regions are now taken to be much larger then their respective minority carrier diffusion lengths.

We now generalize Eq. (1) to cover all dose-rate regimes from low injection to the Auger regime using effective, unified expressions for the minority carrier lifetimes τ_p and τ_n, and for the ambipolar diffusion constants D_{ap} and D_{an} versus dose-rate. For an n-type q-n region, we obtain [12]

$$\tau_p = \left(\frac{1}{\tau_{p1}} + \frac{1}{\tau_{pa}} \right)^{-1}, \tag{6}$$

$$D_{ap} \approx \frac{(n_o + 2G\tau_{p1})D_n D_p}{n_o D_n + (D_n + D_p)G\tau_{p1}}. \tag{7}$$

Here n_o is the majority carrier concentration at thermal equilibrium, D_n and D_p are the electron and hole diffusion constants at low injection, and

$$\tau_{p1} = \frac{1}{2}\left(\tau_{p\infty} - \frac{n_o}{G} \right) + \sqrt{\frac{n_o \tau_{po}}{G} + \frac{1}{4}\left(\tau_{p\infty} - \frac{n_o}{G} \right)^2} \tag{8}$$

is the unified minority carrier lifetime in the SRH regime, from low-level radiation, with lifetime τ_{po}, to saturation of the traps where the lifetime approaches $\tau_{p\infty} \approx \tau_{po} + \tau_{no}$. In the Auger regime, the lifetime approaches

$$\tau_{pa} = \frac{1}{\sqrt[3]{G^2 r_{paug}}}, \tag{9}$$

where r_{paug} is the Auger recombination coefficient.

In Fig. 2, we show the calculated behavior of τ_p and D_{ap} versus the e-h generation rate G for n-type silicon with a doping density of 10^{22} m^{-3}. In Fig. 2a, the various radiation dose-rate regimes and the transition between them are clearly discerned.

In the above discussion, we did not explicitly consider the effect of the electrical field term (ohmic field and internally generated field) [7], [8] in the ambipolar transport equation. This term is mostly important in the transition region between the low-injection and the SRH saturation regimes. At low dose-rates, the electrical field is small, and at higher dose-rates, the ambipolar mobility vanishes [11]. However, since the transition regions are described by interpolation functions, we may considerer the electrical field effect to be contained in these expressions through a suitable adjustment of the parameters.

B. Dynamic Model

To establish a dynamic electrical equivalent of the photocurrent effect for use in SPICE, we write the e-h generation rate as $G(t) = kV_G(t)$ where $V_G(t)$ is a fictitious time-dependent voltage and k is the conversion factor discussed earlier. Any change in the generation rate will set up a transient build-up or discharge of minority carriers in the quasi-neutral regions adjacent to the p-n junction. This variation in the carrier populations are characterized by delays determined by the effective lifetimes τ_{pd} and τ_{nd} of the minority carriers in

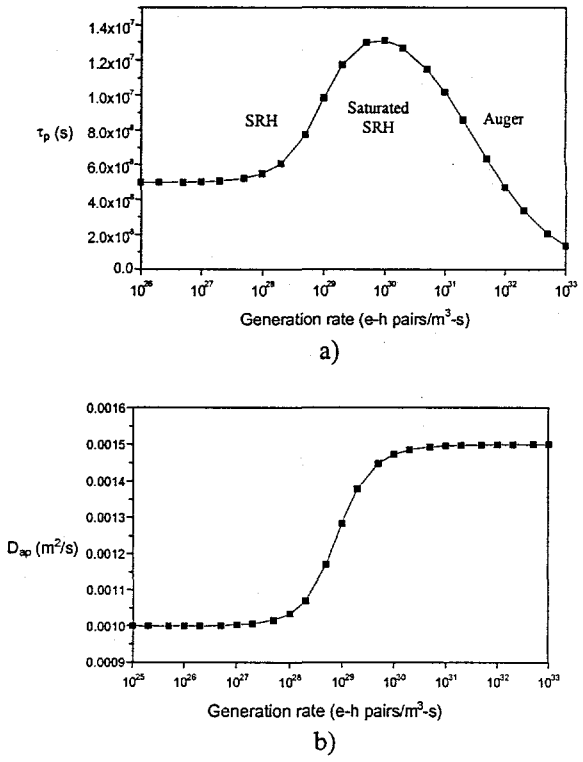

Fig. 2. Examples of unified lifetime τ_p (a) and ambipolar diffusion coefficient D_{ap} (b) versus e-h generation rate G for n-type silicon with a doping density of 10^{22} m^{-3}. For silicon, the generation rates shown can be converted to dose-rates (in rad/s) by dividing G by 4.3×10^{19}.

the n- and p-type regions, approximately given by [12]

$$\tau_{pd} = L_{pd}^2 / D_{ap}, \qquad \tau_{nd} = L_{nd}^2 / D_{an}. \tag{10}$$

In the general case, the effective delay times change continually throughout the transient as a consequence of the dependence of the transport coefficients on the amount of minority carriers within the collection volume.

In SPICE, the delay times may be represented in terms of equivalent circuits such as the one shown in Fig. 1c, which describe the temporal evolution of the total amount of excess minority carriers in the q-n regions. In this model, the dynamic "voltages" V_{Gp} and V_{Gn} represent effective e-h generation rates G_p and G_n, which relate directly to the momentary amount of excess minority carriers within the collection volumes of the q-n regions. Hence, replacing G by G_p and G_n in the second and third terms, respectively, of the total stationary photocurrent in Eq. (1), we obtain the corresponding transient photocurrent given by:

$$I_G = qA(GW_{dep} + G_p L_{pd} + G_n L_{nd}). \tag{11}$$

Note that the effective diffusion lengths L_{pd} and L_{nd} (see Eqs. (2) - (5)) are now dynamic quantities that depend on G_p and G_n, respectively. SPICE determines simultaneously by iteration the "voltages" V_{Gp}, V_{Gn} and the delays τ_{pd}, τ_{nd} of the subcircuit in Fig. 1 at each time step of a transient analysis. The iteration starts from the values determined in the previous time step. At the first time step, the following initial values

apply: $V_{Gp} = V_{Gn} = V_G(0)$, where $V_G(0) = G(0)/k$ corresponds to an initial steady state radiation dose-rate.

C. Geometrical Effects

Fig. 3 shows a schematic cross-section of an n^+-p-p^+ diode, which can be fabricated by epitaxy and diffusion or ion implantation. This figure may also serve as an illustration of the base-collector junction geometry of a BJT. In all but the highest radiation intensities, the vertical collection volume will be significantly reduced by the presence of a Hi-Lo junction, with a penetration of about one diffusion length L_{an+} into the p^+ region (see Eq. 5).

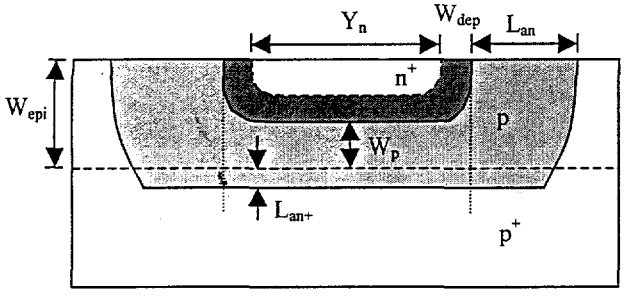

Fig. 3. Schematic cross-section of an n^+-p-p^+ diode. The dark shaded area is the depletion region of width W_{dep}. The lighter shaded region represents the collection volume on the p-side. The dashed horizontal line indicates the metallurgical Hi-Lo junction.

However, as indicated in Fig. 3, this effect may not be present in the lateral extension of the collection volume in the low-doped p-region. In the latter case, the collection volume can be divided into two parts; one between the vertical dotted lines of Fig. 2, which can be described according to the one-dimensional model discussed above, and the remainder constituting the lateral extension region. In the former, the cross-section to be used in Eqs. (1) and (11) is given by

$$A = (Z_n + 2W_{dep})(Y_n + 2W_{dep}), \qquad (12)$$

where the geometrical quantities Y_n and W_{dep} are defined in Fig. 2. Z_n is the extent of the n^+ region in the direction, perpendicular to the plane of the cross-section.

In the one-dimensional model, the photocurrent is proportional to the collection volume. This is also a reasonable approximation for the photocurrent contribution of the lateral extension region, whose volume is

$$V_{ext} \approx 2L_{an}(Z_n + Y_n + 4W_{dep} + 2L_{an})(W_{epi} + L_{an+}) \qquad (13)$$

Here it is assumed that the collection volume extends into the p^+-region. If this is not the case, we may replace the factor $(W_{epi} + L_{an+})$ by $(W_{epi} - W_p + L_{an})$.

We note that the two photocurrent contributions will have different delay times owing to the difference in their effective diffusion lengths.

D. Biasing Effects

The photocurrent generated by radiation will flow through the impedances of the external circuit and those of the device itself, and will therefore contribute to a bias change across the intrinsic device. In a p-n junction, this bias change corresponds to a reduction in the junction barrier, which will give rise to a secondary photocurrent that will add to the primary photocurrent.

Likewise, for a BJT with a base resistance, the base photocurrent causes a reduction in the base-emitter junction barrier, which results in an increased carrier injection from the emitter. Hence, this mechanism provides a considerable addition to the collector photocurrent, corresponding to the primary base photocurrent multiplied by the common-emitter gain (forward active mode). The voltage drop across the collector resistance owing to the collector photocurrent causes a reduction in the reverse bias of the collector junction. At very large photocurrents, this may even forward bias the junction, at which point the collector photocurrent saturates.

In a SPICE simulation, these contributions will automatically be accounted for. However, for a given p-n junction, the bias dependencies of the depletion width W_{dep} and its penetrations x_p and x_n into the p- and the n-regions, respectively, have to be specifically included in the photocurrent model implementation. For abrupt junctions, we have:

$$x_p = \sqrt{\frac{2\varepsilon_s(V_{bi} - V)}{qN_a(1 + N_a/N_d)}}, \quad x_n = \sqrt{\frac{2\varepsilon_s(V_{bi} - V)}{qN_d(1 + N_d/N_a)}} \qquad (14)$$

where ε_s is the dielectric permittivity of the semiconductor, V_{bi} is the built-in voltage of the junction, V is the intrinsic voltage across the diode, N_a is the doping in the p-region, and N_d is the doping of the n-region. The total depletion width is $W_{dep} = x_p + x_n$. Note that for a region with a Hi-Lo junction, the penetration of the depletion width into this region may be effectively limited to the width of the low-doped part. For graded junctions, alternative expressions to those of Eq. (14) should be used [10].

III. SIMULATION RESULTS

The present models were implemented in AIM-Spice [11], [13] and dynamic simulations were performed for diodes and BJTs at different bias configurations, applying radiation pulses between 50 ns and 0.5 μs duration at different dose-rates. For simplicity, only one-dimensional models are considered here.

A. Diode Simulations

The parameters for the n-p and the n-p-p^+ diode simulations are shown in Table 1. The area of the diodes is taken to be 1 mm^2. For simplicity, a bias voltage of 0 V was assumed and the series resistances in the diode and in the external circuit were taken to be 0 Ohm. These idealized (intrinsic) conditions are chosen for the purpose of verifying the correctness of the model implementation in SPICE, since a series resistance will cause a saturation of the photocurrent at large dose-rates. The simulation results for the two diode structures are compared for pulse dose-rates of 10^7 rad/s (Fig. 4a), 10^{10} rad/s (Fig. 4b), and 10^{13} rad/s (Fig. 4c). These dose-rates correspond to the three dose-rate regimes indicated in Fig. 2a. In Figure 5, examples of photocurrent responses are shown in a semilog plot to

emphasize the time constants in the recovery phase of the *n-p* diode.

The following comments apply to the simulation results:

TABLE I
SIMULATION PARAMETERS FOR *N-P* AND *N-P-P*$^+$ DIODES

Diode parameters	Value
Pulse rise time	5e-9 s
Pulse fall time	5e-9 s
Pulse width	5e-8 s, 5e-7 s
Pulse dose-rate	1e7 - 1e13 rad/s
r_{aug}, electrons in *p*-region	1.1e-42 m^6/s
r_{aug}, holes in *n*-region	3e-43 m^6/s
N_i intrinsic carrier conc.	1.45e16 m^{-3}
n-region of n-p-p$^+$ or n-p diode	
N_d	1e25 m^{-3}
W_n	2e-6 m
D_n	2.35e-4 m^2/s
D_p	1.58e-4 m^2/s
τ_{po}	1e-8 s
$\tau_{p\infty}$	2e-8 s
p-region of n-p or n-p-p$^+$ diode	
N_a	5e20 m^{-3}
W_p	5e-5 m, 2e-6 m
D_n	3.45e-3 m^2/s
D_p	1.28e-3 m^2/s
τ_{no}	1e-7s
$\tau_{n\infty}$	2e-7 s
p$^+$-region of n-p-p$^+$ diode	
N_{a+}	1e24 m^{-3}
W_{p+}	5e-5 m
D_{n+}	6.55e-4 m^2/s
D_{p+}	4.63e-4 m^2/s
τ_{no+}	2e-8 s
$\tau_{n\infty+}$	4e-8 s

i) A discontinuity can be discerned in some of the response curves at the start and at the end of the applied radiation pulse. This is a consequence of the sudden onset and termination of the prompt photocurrent.

ii) We note that the total length of the *p*-region of the *n-p* diode is 50 μm, which is larger than the low-injection diffusion length in the low-doped *p*-type material ($L_{no} = \sqrt{D_n \tau_{no}} \approx 19$ μm). From Fig. 5a (left), we find that the recovery delay time for this diode is 8x10^{-8}s at a dose-rate of 10^7 rad/s, which agrees quite well with the delay time calculated from Eqs. (3) and (10) for the low injection case.

iii) As expected, Fig. 4 (left) shows that the recovery time of the *n-p* diode increases with increasing dose-rate between 10^7 and 10^{10} rad/s owing to the saturation of the SRH traps. Figure 4c (left) shows that the overall delay time at the dose rate of 10^{13} rad/s appears to be very much reduced compared to those of the lower dose-rates. This is caused by the initial dominance of rapid Auger recombination. However, the 10^{13} rad/s curve in Fig. 5 (right) reveals that after this initial phase of rapid decay, the recovery enters the saturated SRH regime, where a longer time constant of 1.5x10^{-7}s is found. As the e-h population decreases further, the diode enters the low-injection regime where the time constant is reduced to that of the 10^7 rad/s plot, in agreement with the delay time calculated above.

iv) In the *n-p-p*$^+$ diode, the reduction in the recovery times because of the Hi-Lo junction is quite noticeable. In this case, the delay time is determined by the diffusion across the narrow, low-doped *p* region and by diffusion in the highly doped *p*$^+$

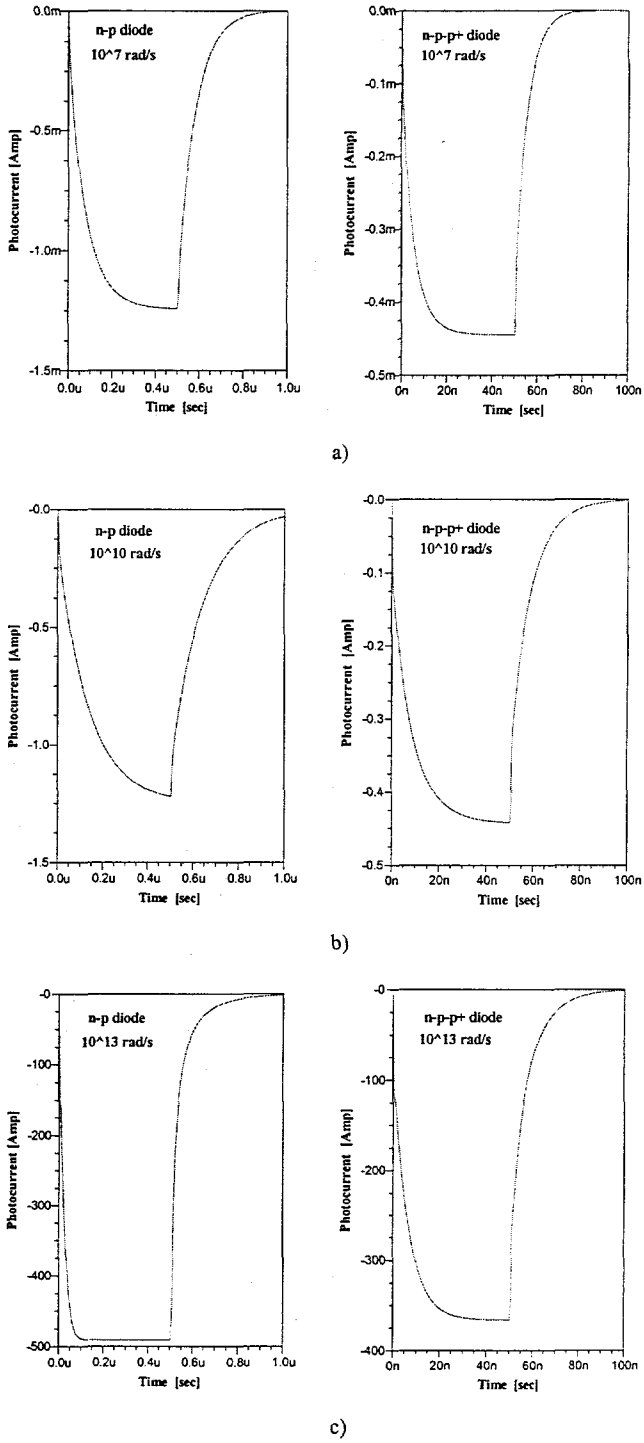

Fig. 4. Transient photocurrent in *n-p* (left) and *n-p-p*$^+$ (right) diodes for radiation pulses of 500 ns and 50 ns, respectively. The dose-rates are 10^7 rad/s (a), 10^{10} rad/s (b), and 10^{13} rad/s (c). Note the time scale difference between the *n-p* and *n-p-p+* diodes.

region. We also notice a reduction in the peak photocurrents compared with those of the *n-p* diode owing to the smaller

collection volume of the n-p-p^+ diode.

v) The results obtained from the diode simulations are very much dependent on the choice of parameters used. These parameters have to be carefully selected based on the proper-

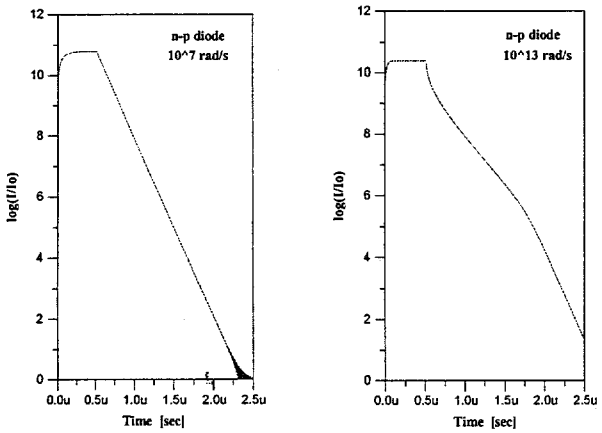

Fig. 5. Transient photocurrents as in Fig. 4, shown in a semilog scale (base 10) to reveal the recovery time constants.

ties of the materials and on the geometry of the device. As demonstrated above, delay times can ideally be extracted from the response curves, allowing, in principle, some of the dominant diode parameters (lifetimes and diffusion coefficients) to be determined from experiments.

TABLE 2
SIMULATION PARAMETERS FOR *BJTS*

BJT Parameters	Value
Pulse rise time	5e-9 s
Pulse fall time	5e-9 s
Pulse width	2e-7 s
Pulse dose-rate	1e7-1e13 rad/s
n^+-emitter	
N_d	1e25 m^{-3}
W_n	2e-6 m
D_n	6e-4 m^2/s
D_p	2e-4 m^2/s
τ_{po}	2e-8 s
$\tau_{p\infty}$	4e-8 s
p-base	
N_a	1e22 m^{-3}
W_b	1e-6 m
D_n	3e-3 m^2/s
D_p	1.5e-3 m^2/s
τ_{no}	1e-7 s
$\tau_{n\infty}$	2e-7 s
n-collector or n^--region of Hi-Lo collector	
N_d	5e20 m^{-3}
W_p	5e-5 m, 4e-6 m
D_n	6e-3 m^2/s
D_p	2e-3 m^2/s
τ_{po}	1e-6 s
$\tau_{p\infty}$	2e-6 s
n^+- region of Hi-Lo collector	
N_d	1e24 m^{-3}
W_p	5e-5 m
D_n	2.5e-3 m^2/s
D_p	5e-4 m^2/s
τ_{po}	1e-7 s
$\tau_{p\infty}$	2e-7 s

B. BJT Simulations

To test the BJT model, we considered one-dimensional n-p-n transistors with and without a Hi-Lo junction in the collector. The substrate effects were neglected. Radiation pulses of 200 ns at different dose-rates were applied, using the pulse shape defined in Table 2. In the simulations, a base-emitter voltage V_{be} of 0.7 or 1 V and a collector-emitter voltage V_{ce} of 4 V were assumed. Both the base resistance R_b and the collector resistance R_c were varied. The radiation related device parameters used in the simulation are also shown in Table 2.

Examples of simulated base and collector transient photocurrents for the two BJT structures are shown for various pulse dose-rates in Figs. 6 and 7 (intrinsic photocurrent)) and in Fig. 8 (with series resistances).

The following comments apply to the simulation results:

i) In the simulations of Fig. 6 for a BJT with a uniformly doped collector, the external and internal circuit resistances are set to zero. Thereby, we eliminate the photovoltaic effect and the secondary photocurrent, allowing us to observe the intrinsic (primary) photocurrent response. We note that the uniform, low-doped collector results in relatively long rise and fall times in the response at the lowest dose-rates (10^7 rad/s shown in Fig. 6 (left)). A delay time in the recovery of about 2×10^{-7} s is found from the semilog plot in Fig. 6c (left). However, at the highest dose-rate (10^{13} rad/s shown in Fig. 6 (right)), these times are initially considerably shortened owing to the Auger effect, although the longer time constants are still present in the tail of the recovery as the carrier concentration passes through the various regimes.

We again notice the discontinuities in the response curves at the start and at the end of the applied radiation pulse, owing to the sudden onset and termination of the prompt photocurrent.

ii) Figure 7 shows a similar set of simulations as in Fig. 6 for a BJT with a Hi-Lo collector structure. As expected, this BJT has considerably shorter photocurrent recovery times (by almost a factor of 10) owing to the reduction of the effective carrier diffusion length and of the delay time in the Hi-Lo collector (note the scale change on the time axis between Figs. 6c and 7c).

iii) Figure 8 shows the effects of adding typical intrinsic series resistances (R_b = 10 Ohm, R_c = 1 Ohm) to the base and collector loops of the uniform collector BJT. First of all, the series resistances change the operating point of the transistor, by adjusting the steady-state base and collector currents. In addition, already at the lower dose rate of 10^7 rad/s, the transient photocurrents are significantly changed compared to those of Fig. 6. The base photocurrent is somewhat reduced while the collector photocurrent is increased by nearly an order of magnitude. These effects mainly result from the added voltage drop across R_b, which causes an increase of the forward emitter junction bias and, hence, of the collector

current (secondary photocurrent).

At the higher dose rate of 10^{10} rad/s, the base photocurrent tends to saturate because of the reduced majority carrier lifetime in the base owing to the strong secondary photocurrent. The base current saturation is even more pronounced at the highest dose-rate of 10^{13} rad/s (not shown). In addition, at this dose-rate, we again have the reduced response times owing to Auger recombination.

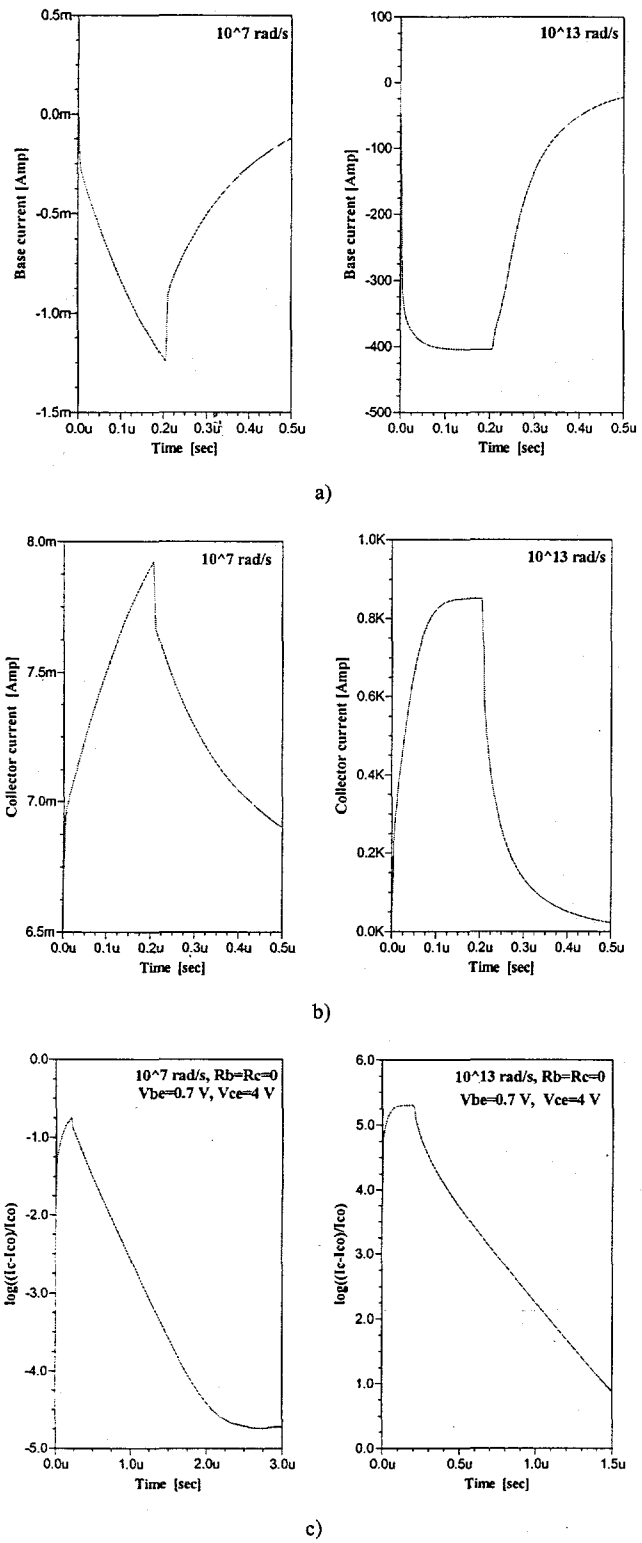

Fig. 6. Intrinsic transient photocurrents in a BJT with uniformly doped collector. The base current (a) and the collector current (b) are shown in a linear scale. The latter is also shown in a semilog (base 10) plot (c). The following parameters are used: V_{be} = 0.7 V, V_{ec} = 4 V, R_b = 0 Ohm, R_c = 0 Ohm, pulse width: 200 ns, dose-rates: 10^7 rad/s (left) and 10^{13} rad/s (right).

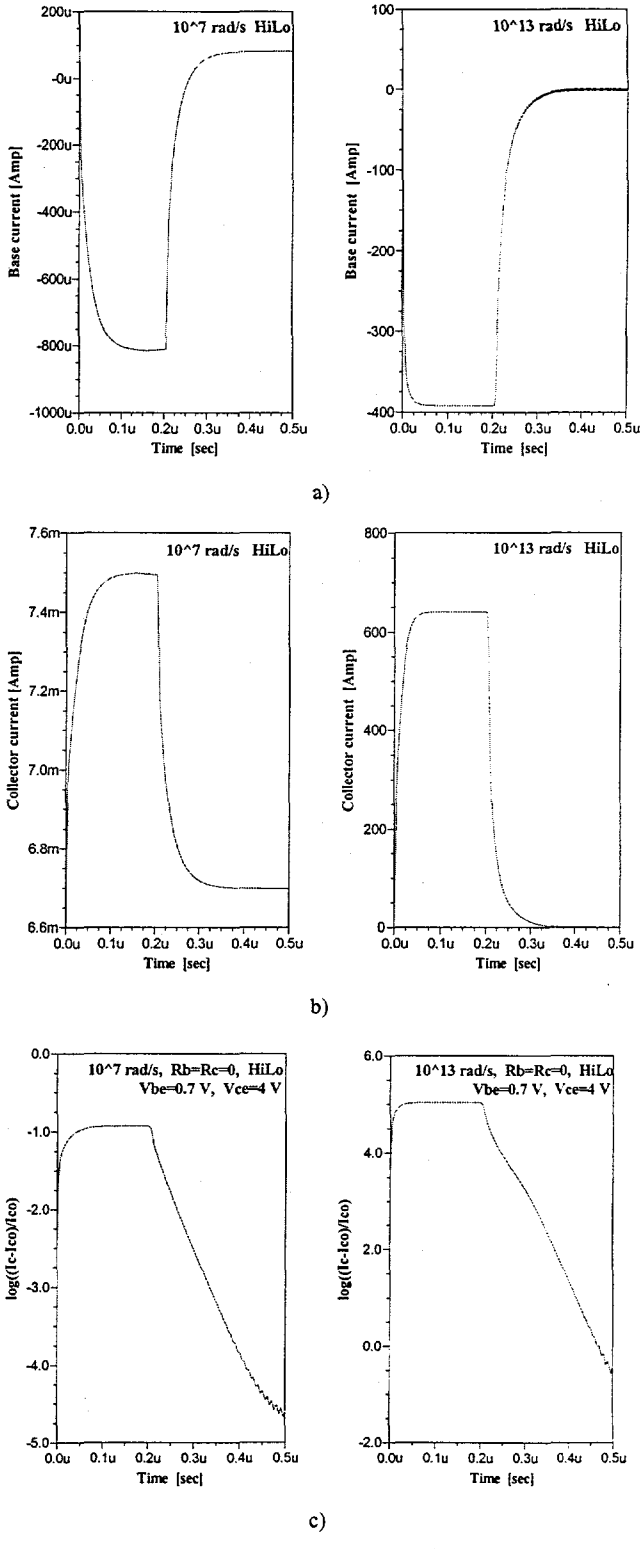

Fig. 7. Intrinsic transient photocurrents in a BJT with Hi-Lo collector. The base current (a) and the collector current (b) are shown in a linear scale. The latter is also shown in a semilog (base 10) plot (c). The following parameters are used: V_{be} = 0.7 V, V_{ec} = 4 V, R_b = 0 Ohm, R_c = 0 Ohm, pulse width: 200 ns, dose-rates: 10^7 rad/s (left) and 10^{13} rad/s (right).

The main effect of R_c is to limit the collector current, as barely seen in the collector response obtained for 10^{10} rad/s. For R_c = 1 Ohm, the collector current is being limited to about 3.3 A because of the induced forward biasing of the collector junction.

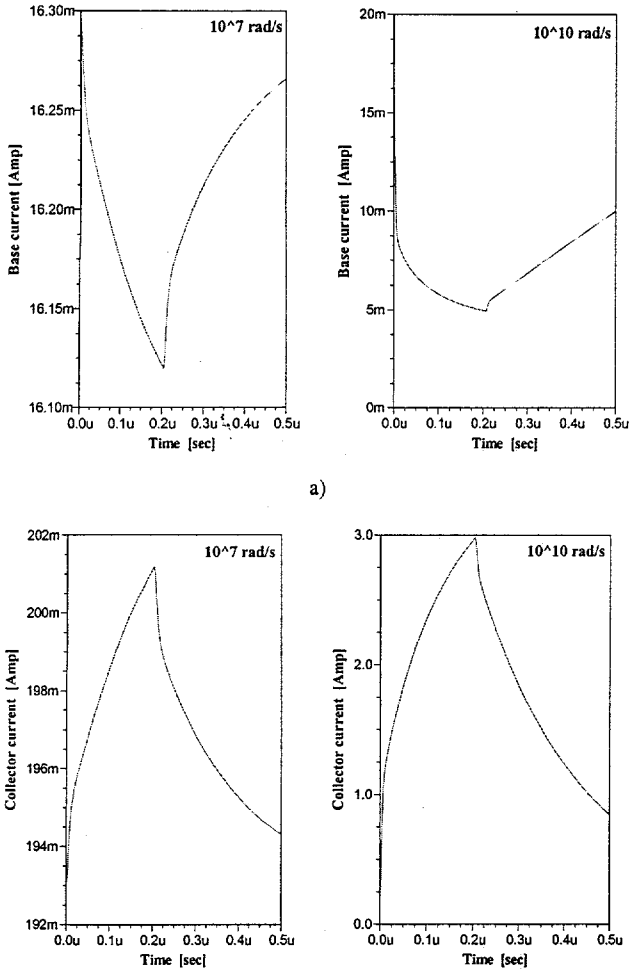

Fig. 8. Transient photocurrents in a BJT with uniform collector. The base current (a) and the collector current (b) are shown for V_{be} = 1 V, V_{ec} = 4 V, R_b = 10 Ohm, R_c = 1 Ohm. The pulse width is 200 ns and the dose-rates are 10^7 rad/s (left) and 10^{10} rad/s (right).

In sum, the above simulations are in good general agreement with expectations, which serve to verify the correctness of the model implementation in AIM-Spice. However, the detailed results are very much dependent on the particular set of parameters used. Hence, for a realistic comparison with experiments or device simulations (such as with MEDICI), these parameters have to be carefully selected to match the properties of the device being investigated. In particular, this means that the geometry, the doping profiles and the electrical characteristics of the device should be known.

IV. MEDICI Simulations

The present model was also verified by comparisons with simulations using the MEDICI device simulator [9]. Figure 9 shows the results for *n-p* and *n-p-p+* diodes for dose-rates of 10^7 and 10^{10} rad/s. (At higher dose-rates, we experienced convergence problems with MEDICI.)

At the outset, the AIM-Spice and MEDICI parameters were basically the same as in Table 1. However, as indicated above, an adjustment is required in some of the AIM-Spice parameters, mainly in the low-injection carrier life-times, in order to obtain a satisfactory correspondence with the MEDICI results. Especially for the *n-p* diode (Fig. 9a), the parameters τ_{po} and τ_{no} of the low-doped regions had to be reduced by about an order of magnitude. Lesser adjustments were needed for the *n-p-p+* diode.

This effect can be explained by the need to account for the electrical field term in ambipolar transport equation at intermediate dose-rates, i.e., at the transition between the low-injection and the saturated SRH regimes. As discussed in Section II, the present model does not explicitly include this effect. Instead, it relies on an interpolation scheme, which requires a suitable adjustment of the SPICE parameters such as the time constants and diffusion constants.

We note that the electrical field will speed up the carrier transport in the q-n regions, especially in regions with low doping, such as the *p*-region of the *n-p* diode. Owing to the much higher doping concentration in the *p+* region of the *n-p-p+* diode, the ambipolar effects are correspondingly weaker

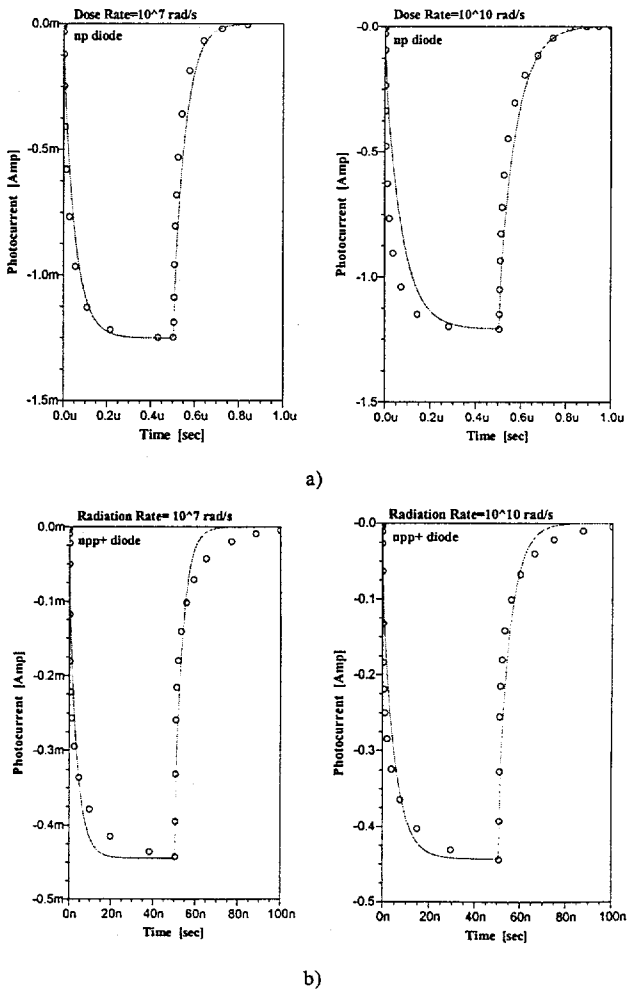

Fig. 9. Comparison of intrinsic transient photocurrents in diodes simulated by MEDICI (symbols) and by AIM-Spice (solid lines). Results are shown for an *n-p* diode wirh a pulse width of 0.5 μs (a) and for an *n-p-p+* diode with a pulse width of 50 ns (b). The dose-rates are 10^7 rad/s (left) and 10^{10} rad/s (right). Bias voltage: 0 V, series resistance: 0 Ohm.

and the need to adjust the parameters is much less in this device.

After performing the necessary parameter adjustments, the present SPICE model shows a satisfactory agreement with the MEDICI calculations. The remaining differences can probably be attributed to additional simplifications done in the present model, as discussed in Section II.

V. Conclusion

We have developed a dynamic SPICE model for the photocurrent response of diodes and BJTs exposed to ionizing radiation. The model is valid for a wide range of dose-rates, up to 10^{13} rad/s. This is achieved by describing the major ambipolar transport parameters in terms of effective, unified quantities, which are valid for the range of dose-rates considered. The major recombination mechanisms, including Schottky-Read-Hall and Auger recombination are also included in the model.

The model describes the prompt photocurrent associated with photogeneration in the junction depletion regions, and the delayed photocurrent associated with the quasi-neutral regions adjacent to the junctions. The diode and the BJT models handle both uniformly doped quasi-neutral regions and regions with a Hi-Lo junction, such as the collector region of BJTs. The model is described in terms of electrical equivalent circuits suitable for implementation in SPICE. The photocurrents are represented by current sources incorporating the transient effects associated with each *p-n* junction. The diode and the BJT models have been implemented in AIM-Spice.

The diode model was verified by comparison with numerical device simulations using MEDICI. Note that this comparison also serves as a verification of the BJT model, since it uses the same basic photocurrent sources as that of the diode.

To further verify the model and adapt it to realistic device structures, we propose that a series of radiation experiments be performed on well-characterized diodes and BJTs, using pulsed gamma or X-ray radiation at a wide range of dose rates. Included in these experiments should also be a study of the total dose effect, which was not a part of the present work. At the highest dose-rates, above about 10^{10} rad/s, even short radiation pulses will permanently degrade and even destroy the devices and thereby strongly affect the observed device response.

Acknowledgment

This work was supported by Sandia National Laboratories under Contact No. A30259. We acknowledge the valuable discussions with several scientists at Sandia, including Wendland Beezhold, Carl Axness, Carolyn Bogden and Regina Schells.

References

[1] T. P. Ma and P. V. Dressendorfer, *Ionizing Radiation Effects in MOS Devices and Circuits*. New York, NY: John Wiley & Sons, 1989.

[2] G. C. Messenger and M. S. Ash, *The Effects of Radiation on Electronic Systems*. New York, NY: Van Nostrand Rheinhold, 1992.

[3] J. L. Wirth and S. C. Rogers, "Transient radiation current generator model for semiconductor devices," *IEEE Trans. Nuc. Sci.*, vol. 11, pp. 24-38, 1964.

[4] J. R. Florian, R. W. Jacobs, P. E. Micheletti, and E. E. King, "Improved transient response modeling in IC's," *IEEE Trans. Nuc. Sci.*, vol. 31, no. 6, Dec. 1984.

[5] D. Long, J. Florian, and R. Casey, "Transient response model for epitaxial transistors," *IEEE Trans. Nuc. Sci.*, vol. 30, no. 6, pp. 4131-4134, 1983.

[6] E. W. Enlow and D. R. Alexander, "Photocurrent modeling of modern microcircuit p-n junctions," *IEEE Trans. Nuc. Sci.*, vol. 34, no. 6, pp. 1467-1474, 1988.

[7] T. F. Wunsch and C. L. Axness, "Modeling of time-dependent transient radiation response of semiconductor junctions," *IEEE Trans. Nuc. Sci.*, vol. 39, no. 6, Dec. 1992.

[8] A. N. Ishaque, J. W. Howard, M. Becker, and R. C. Block, "Photocurrent modeling at high dose rates," *IEEE Trans. Nuc. Sci.*, vol. 36, no. 6, Dec. 1989.

[9] MEDICI by Avant! Corporation, see http://www.avanticorp.com/

[10] S. M. Sze, *Physics of Semiconductor Devices*, 2nd ed., New York, NY: John Wiley & Sons, 1981.

[11] T.A. Fjeldly, T. Ytterdal and M. Shur, *Introduction to Device Modeling and Circuit Simulation*. New York, NY: John Wiley & Sons, 1998.

[12] T.A. Fjeldly, Y. Deng and M. Shur, *Physics Based Modeling of High Intensity Ionizing Radiation Effects in Bipolar Junction Transistors*, unpublished.

[13] AIM-Spice, see: http://www.aimspice.com